THE GEORGE WASHINGTON UNIVERSITY

THE GELMAN LIBRARY SYSTEM

You have received this document through Gelman Library's Interlibrary Loan Office.

If you notice any errors in its quality or otherwise, please contact us at *ill@gwu.edu* or 202-994-7128.

This document will be removed from MyAladin in 14 days.

Thank you for using our service!

Notice:
Warning Concerning Copyright Restrictions

The copyright law of the United States (Title 17, United States Code) governs the making of photocopies or other reproductions of copyrighted material.

Under certain conditions specified in the law, libraries and archives are authorized to furnish a photocopy or other reproduction. One of these specific "fair use" conditions is that the photocopy or reproduction is not to be "used for any purpose other than private study, scholarship, or research." If a user makes a request for, or later uses, a photocopy or reproduction for purposes in excess of "fair use," that user may be liable for copyright infringement.

No further reproduction and distribution of this copy is permitted by transmission or any other means.

This article was downloaded by: [University of Delaware]
On: 16 October 2014, At: 07:55
Publisher: Taylor & Francis
Informa Ltd Registered in England and Wales Registered Number: 1072954 Registered office: Mortimer House, 37-41 Mortimer Street, London W1T 3JH, UK

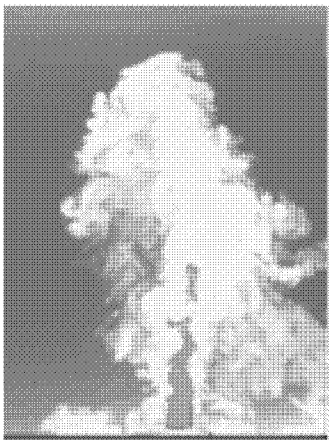

Journal of Turbulence
Publication details, including instructions for authors and subscription information:
http://www.tandfonline.com/loi/tjot20

Effects of dimples on laminar boundary layers

N. Beratlis[a], E. Balaras[b] & K. Squires[a]

[a] Department of Mechanical and Aerospace Engineering, Arizona State University, Tempe, AZ, USA

[b] Department of Mechanical and Aerospace Engineering, The George Washington University, Washington, DC, USA

Published online: 12 Jun 2014.

To cite this article: N. Beratlis, E. Balaras & K. Squires (2014) Effects of dimples on laminar boundary layers, Journal of Turbulence, 15:9, 611-627, DOI: 10.1080/14685248.2014.918270

To link to this article: http://dx.doi.org/10.1080/14685248.2014.918270

PLEASE SCROLL DOWN FOR ARTICLE

Taylor & Francis makes every effort to ensure the accuracy of all the information (the "Content") contained in the publications on our platform. However, Taylor & Francis, our agents, and our licensors make no representations or warranties whatsoever as to the accuracy, completeness, or suitability for any purpose of the Content. Any opinions and views expressed in this publication are the opinions and views of the authors, and are not the views of or endorsed by Taylor & Francis. The accuracy of the Content should not be relied upon and should be independently verified with primary sources of information. Taylor and Francis shall not be liable for any losses, actions, claims, proceedings, demands, costs, expenses, damages, and other liabilities whatsoever or howsoever caused arising directly or indirectly in connection with, in relation to or arising out of the use of the Content.

This article may be used for research, teaching, and private study purposes. Any substantial or systematic reproduction, redistribution, reselling, loan, sub-licensing, systematic supply, or distribution in any form to anyone is expressly forbidden. Terms & Conditions of access and use can be found at http://www.tandfonline.com/page/terms-and-conditions

Journal of Turbulence, 2014
Vol. 15, No. 9, 611–627, http://dx.doi.org/10.1080/14685248.2014.918270

Taylor & Francis
Taylor & Francis Group

Effects of dimples on laminar boundary layers

N. Beratlis[a]*, E. Balaras[b] and K. Squires[a]

[a]*Department of Mechanical and Aerospace Engineering, Arizona State University, Tempe, AZ, USA;* [b]*Department of Mechanical and Aerospace Engineering, The George Washington University, Washington, DC, USA*

(*Received 17 December 2013; accepted 22 April 2014*)

A series of direct numerical simulations of the flow past a flat plate with two and eight rows of dimples in a staggered arrangement is carried out. The Reynolds number based on the boundary layer thickness and freestream velocity near the inflow plane is 1000 and the dimples are spherical with a depth to diameter ratio of 0.1. The incoming flow is laminar and the boundary layer thickness before the dimples is half the dimple depth. At this low Reynolds number the flow is expected to remain laminar over a smooth flat plate. The presence of the dimples triggers instabilities that cause significant momentum transport. It is shown that the shear layer that forms as the flow separates over the first two rows of dimple becomes unstable and sheds coherent vortex sheets. The vortex sheets become unstable and are transformed into packets of horseshoe vortices. When these vortices evolve over a flat plate or over a series of dimples the flow dynamics are very different with important changes in momentum transport across the boundary layer.

Keywords: dimples; flat plate; transition; shear layer; momentum transport; laminar; turbulent

Downloaded by [University of Delaware] at 07:55 16 October 2014

1. Introduction

Passive roughness elements such as trip wires, dimples, sand-grain roughness, etc., have been shown to be effective in reducing drag on bluff (i.e. sphere, cylinder) as well as streamlined (i.e. airfoils) bodies (see [1] for a review). The type and arrangement of these elements on the surface of the body plays an important role in the process. For the case of a bluff body, such as a sphere, an example is shown in Figure 1, where the variation of the drag coefficient, C_D, as a function of Reynolds number (based on the freestream velocity, U_∞, and the sphere diameter, D) is shown for smooth and rough spheres. For the former case the drag coefficient remains constant ($C_D \sim 0.5$) until the Reynolds number approaches a critical value ($\mathrm{Re} \sim 2 \times 10^5$). At this point, which is usually referred to as *drag crisis*, C_D decreases rapidly and hits a minimum, which is an order of magnitude lower ($C_D \sim 0.05$). Further increase in the Reynolds number results in a small increase of C_D.

For the case of rough spheres the critical Reynolds number is around or below $\mathrm{Re} = 10^5$, and decreases with increasing roughness height, k. In this case, however, the minimum drag coefficient is higher than the one for a smooth sphere, and increases with increasing k. It can also be seen that in the post-critical regime, the drag coefficient quickly increases with the Reynolds number to a value of $C_D = 0.4$. It has been conjectured that this is due to

*Corresponding author. Email: nikos.beratlis@gmail.com

© 2014 Taylor & Francis

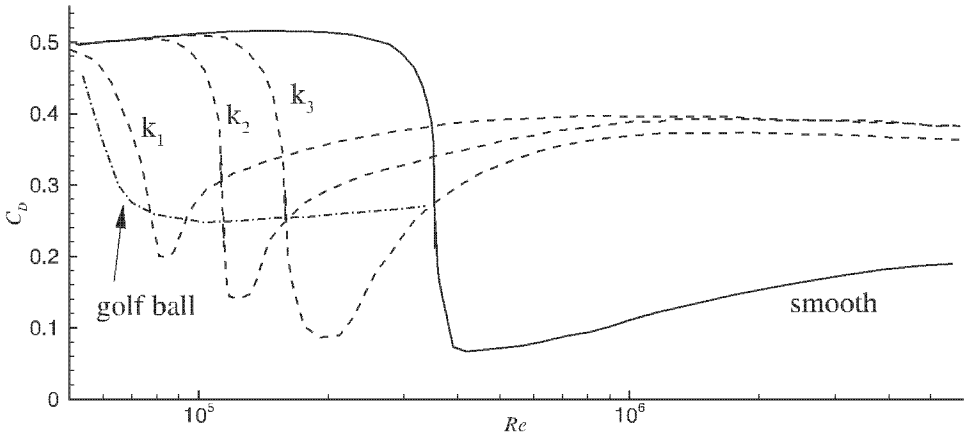

Figure 1. Drag coefficient, C_D, as a function of the Reynolds number, Re, for various spheres. —— smooth sphere [2]; – – – rough spheres of varying roughness height ($k_1/D = 1250 \times 10^{-5}$, $k_2/D = 500 \times 10^{-5}$, $k_3/D = 150 \times 10^{-5}$, where k is the roughness height and D is the diameter of the sphere) [2]; – · – dimpled sphere [3].

the characteristics of the boundary layer developing over sand-grain roughness: sand-grain roughness induces transition to turbulence of the incoming laminar boundary layer, which then quickly thickens over the rough surface, reducing the near-wall momentum. As a result it separates earlier, increasing the pressure drag. This is consistent with the measurements in [2].

For the case of dimpled spheres similar behaviour has been observed: the critical Reynolds number decreases as the dimple depth increases. The minimum C_D decreases by as much as 50% compared to the smooth sphere at the same Reynolds number, but is higher than the one obtained with sand-grain roughness of equivalent height. In the post-critical regime, however, the drag coefficient remains approximately constant for a wide range of Reynolds numbers. Choi et al. [4] conjectured that the drag coefficient remains constant because the separation point is fixed for a wide range of Reynolds numbers, as demonstrated by oil visualisations in their experiments. They also showed that the Reynolds number affects only the location of the initial instability: as the Reynolds number increases the location where the incoming flow becomes unstable moves closer to the stagnation point at the front of the sphere.

The above results indicate that the turbulent boundary layer like flow, induced by sand-grain roughness is different from the one generated by the dimples.

In the latter case, it has been shown that turbulence is generated by a shear layer instability just above the dimples, which dominates the momentum transfer near the wall (transfers high-speed fluid towards the surface of the sphere) [4]. Further support for this mechanism was provided by recent direct numerical simulations (DNS) in [5]. In the case of sand-grain roughness, on the other hand, it is conjectured that a more *canonical* turbulent boundary layer over a rough wall is formed.

Today, the details of the structure and evolution of the turbulent-like boundary layers induced by different types of roughness elements are still not very well understood. Although a turbulent boundary layer induced by a finite-length roughness patch will eventually lose memory of the type of roughness, in separation control applications the initial growth of the disturbances and their impact on the momentum distribution normal to the wall are of great

Downloaded by [University of Delaware] at 07:55 16 October 2014

Downloaded by [University of Delaware] at 07:55 16 October 2014

importance. In a dimpled sphere, for example, at super-critical Reynolds numbers, the initial disturbances are generated at the second or third dimple from the stagnation point (depending on the Reynolds number) and in most cases global separation occurs within the first 10 rows of dimples. In general, during this initial growth period the type and arrangement of roughness elements, surface curvature, pressure gradients and the Reynolds number are the primary factors that determine the location of the separation line. The primary objective of the present study is to enhance our understanding of the basic flow physics during the initial stages of the interaction of roughness elements with laminar boundary layers. To reduce the parametric space we will consider a simplified configuration consisting of a flat plate, which is partially covered with roughness elements, with an incoming laminar boundary layer. We will focus on one type of roughness, spherical dimples, which are arranged in one, two and up to eight rows. By varying the length of the roughness patch we will be able to better illuminate its effects on the laminar boundary layer. Although in our configuration the effects of curvature, pressure gradients, etc. are neglected, we will show that our findings are relevant to separation control applications by considering the case of a dimpled sphere with different dimple arrangements.

2. Problem set-up

Figure 2 shows two of the geometries used in this study. They both consist of a flat plate upon which multiple rows of spherical dimples are placed at some distance downstream of the plate origin with an incoming laminar boundary layer. The ratio of the dimple maximum depth, d, to the circumscribed diameter, D, was set to $d/D = 0.1$, which is representative of the typical golf ball used in most of the experimental studies. In one configuration only two rows of dimples in a staggered formation are present (Figure 2(a)) , while in the other case six additional rows of dimples have been added past the second row (Figure 2(b)). Each row is staggered with respect to the previous one. The distance between the centres of adjacent dimples in the spanwise and streamwise directions is $1.1D$ leaving a small gap of $0.1D$ between dimples. In both cases after the last row of dimples the flat plate remains smooth until the end of the computational domain.

The simulations are carried out using finite-difference Navier–Stokes solver. The governing equations for viscous incompressible flow are discretised on a structured grid in Cartesian coordinates. The boundary conditions on the dimpled flat plate, which is not

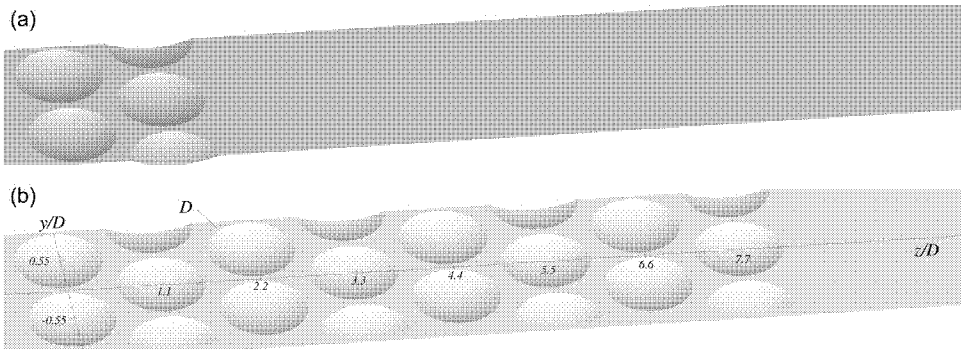

Figure 2. Geometries of a flat plate with (a) two rows of dimples and (b) eight rows of dimples in a staggered arrangement.

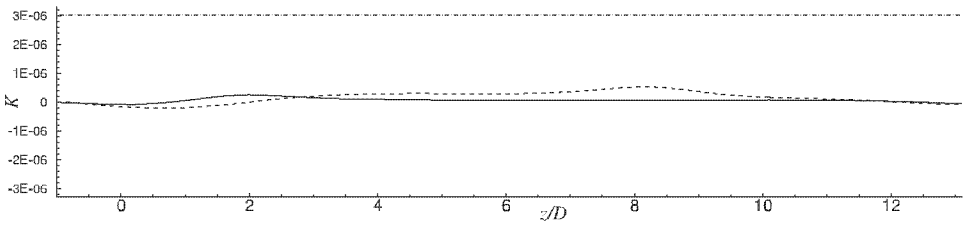

Figure 3. Plot of the time-average acceleration parameter K versus streamwise coordinate z for the case of two rows of dimples. Lines represent: —— two rows of dimples; – – – eight rows of dimples; – · – relaminarisation threshold [9–11].

Downloaded by [University of Delaware] at 07:55 16 October 2014

aligned with the grid lines, are imposed using an immersed-boundary formulation [6]. An exact, semi-implicit, projection method is used for the time advancement. All terms are treated explicitly using the Runge–Kutta third-order scheme, except for the viscous and convective terms in the wall-normal direction which are treated implicitly using a second-order Crank–Nicholson scheme. All spatial derivatives are discretised using second-order central-differences on a staggered grid. The code is parallelised using a classical domain decomposition approach. Details on the overall formulation together with a comprehensive validation study can be sound in [6–8].

For all cases the centre of the dimples in the first row is located at $y/D = \pm 0.55$ and $z/D = 0$ where x, y and z denote the wall-normal, spanwise and streamwise coordinates, respectively. The flat plate is located at $x/d = 1$ and the bottom of the dimples at $x/d = 0$. The domain in y is $2.2D$ and it extends $0.55D$ and $13D$ upstream of the leading edge and downstream of the trailing edge of the first row of dimples, respectively. The top boundary is located at $1.9D$ above the flat plate. At the inlet the Blasius boundary solution is specified. The ratio of the boundary layer thickness, δ, is set in a way that just before the first row of dimples $\delta/d = 0.5$. The Reynolds number based on the boundary layer thickness δ or the momentum thickness θ before the first row of dimples is 1000 and 134, respectively. At the top boundary the wall-normal velocity component obtained from the Blasius solution is specified. This type of boundary condition provides the correct mass flux through the top boundary to account for the Blasius boundary layer growth. In our case, however, due to the presence of the dimples and the fact that the flow downstream is not laminar, it may introduce a pressure gradient resulting in freestream acceleration. To quantitatively assess to what extent this happens in our computations, the acceleration coefficient, $K = -(\nu/U_\infty^2)(dU_\infty/dz)$ was computed at the top boundary (ν is the kinematic viscosity of the fluid, U_∞ is the freestream velocity and z is the coordinate in the streamwise direction). K for the two cases is shown in Figure 3. The highest value of acceleration coefficient was found to be 2.5×10^{-7} and 5.0×10^{-7} for the two and eight rows of dimples, respectively, pointing to the presence of a very mild pressure gradient, which is not expected to affect the flow [9–11]. At the outlet a convective boundary condition is used, while periodic boundary conditions are used in the spanwise direction.

The computational grid, which is designed to resolve both the shear layer dynamics in the vicinity of the dimple and the turbulent-like boundary layers forming downstream of the dimples, is stretched in the wall-normal and streamwise directions. In particular, in the post-dimple region the grid spacings in wall units are $\Delta x^+_{\min} = 0.34$ for the first cell away from the flat plate, uniform $\Delta y^+ = 6.5$ and $\Delta z^+_{\max} = 11$ based on the location and value of the maximum wall shear velocity. In the dimples there are approximately 90 points across their maximum depth, 120 points in the streamwise direction between their trailing

Downloaded by [University of Delaware] at 07:55 16 October 2014

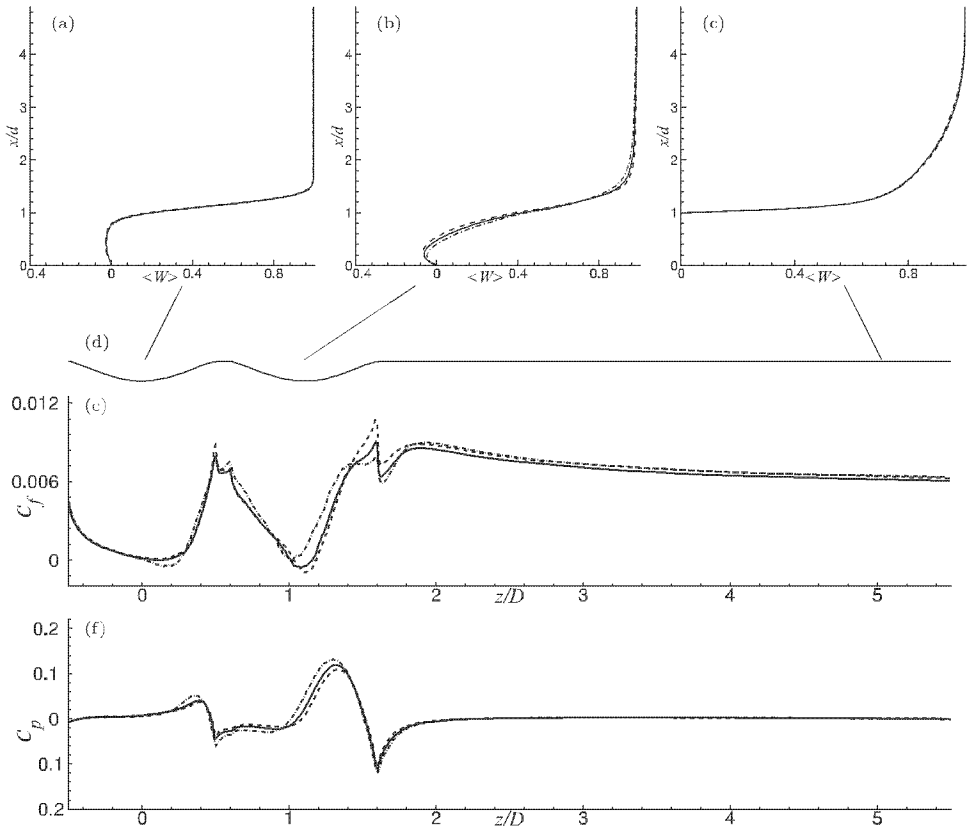

Figure 4. (a)–(c) Profiles of the streamwise velocity $<W>$ averaged over both time and spanwise direction. (d) Outline of the location of the flat surface averaged over the spanwise direction. The three locations corresponding to the velocity profiles above are shown. Plot of (e) the skin friction coefficient $<C_f>$ and (f) pressure coefficient $<C_p>$ along $x/d = 1$, both averaged over both time and spanwise direction versus streamwise coordinate. Lines represent: – – – finer grid; —— reference grid; —·— coarser grid.

and leading edges and 220 points across their diameter in the spanwise direction. The total number of grid points utilised for all cases is 394 × 452 × 1552, in the wall-normal, spanwise and streamwise directions, respectively.

To demonstrate that the results are grid independent a grid refinement study was performed for the case of the two rows of dimples. In the study the domain in the streamwise direction was shorter and extended approximately $5.5D$ downstream of the trailing edge of the second row of dimples. Three different grids were employed; the reference grid with exactly the same grid resolution in each coordinate as the grid used throughout this paper, and a coarser and a finer grid with approximately 50% less and more points in each direction than the reference grid, respectively. Figure 4(a)–(c) shows profiles of the streamwise velocity averaged over both time and spanwise direction at three locations: two corresponding to the middle of the first and second rows of dimples, respectively, and one at $z/D = 5D$ located in the post-dimple region. The agreement between all grids is very good. The skin friction coefficient, $<C_f>$, for the three grids is shown in Figure 4(d). The coarser grid shows some deviation from the other two grids within the dimples, but the

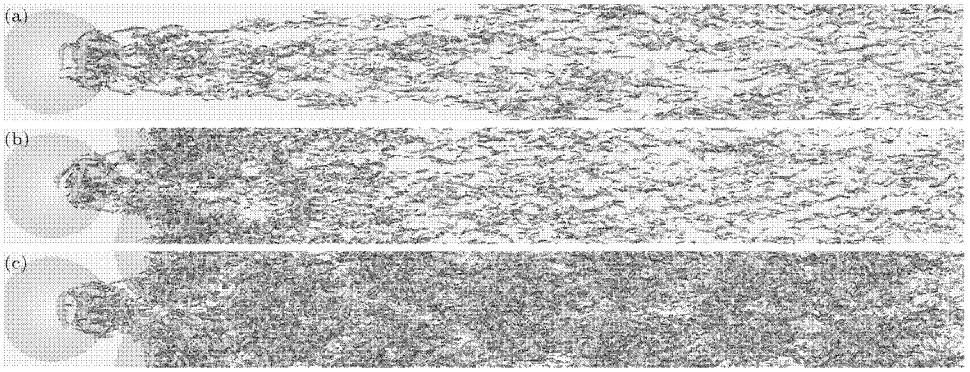

Figure 5. Top view of an instantaneous snapshot of the near-wall vortices visualised using Q isosurfaces coloured by the streamwise vorticity. (a) one row, (b) two rows and (c) eight rows of dimples.

Downloaded by [University of Delaware] at 07:55 16 October 2014

reference grid agrees well with the finer grid: the only difference is the peak of $<C_f>$ which is slightly underpredicted at the trailing edge of the second row of dimples. In the post-dimple region the agreement among all grids is excellent. The pressure coefficient, $<C_p>$, shown in Figure 4(f) behaves in a similar manner and the differences between the two finer grids are very small.

All simulations were initialised with the Blasius solution and initial integration of approximately $400D/U$ time units was found to be necessary to reach a state that does not depend on initial conditions. Statistics were then accumulated over $500D/U$ time units with a time step of $0.4e-1D/U$. In some of the plots shown in this paper statistics have been also ensemble-averaged in the spanwise direction. A variable U that has been averaged over time is denoted as $\overline{U}$ while a variable averaged over time and over the spanwise direction is denoted by $<\overline{U}>$.

3. Results

3.1. *Instantaneous flow structures*

In this section we will focus primarily on the differences between the two cases we considered in this study: the flow downstream of two rows of dimples in a staggered arrangement, referred to as *case 1* from now on; and *case 2*, where we have introduced six additional rows of dimples in a staggered arrangement downstream of the first two rows (see Figure 2). The first two rows of dimples introduce a perturbation to the incoming laminar boundary layer, which then evolves over a smooth surface (case 1), or a dimpled surface (case 2). In Figure 5 an instantaneous snapshot of the vortical structures, visualised using the second invariant of the velocity gradient tensor, Q, is shown [12]. The vortices are coloured by the streamwise vorticity, ω_z. In both cases the disturbance generated by the first two rows of dimples is similar: as the flow goes over the first row of dimples it separates and forms a shear layer which rolls up into a coherent roller. The roller initially contains mainly spanwise vorticity, but as it evolves it undergoes a complex three-dimensional instability above the dimples converting its spanwise vorticity into streamwise vorticity. The similarities, however, end at the second row of dimples. Beyond this point for case 1 one can see typical quasi-streamwise vortices reminiscent of turbulent boundary layers, while for case 2 the near-wall vortex dynamics appear to be more complex. A flow visualisation of the case of

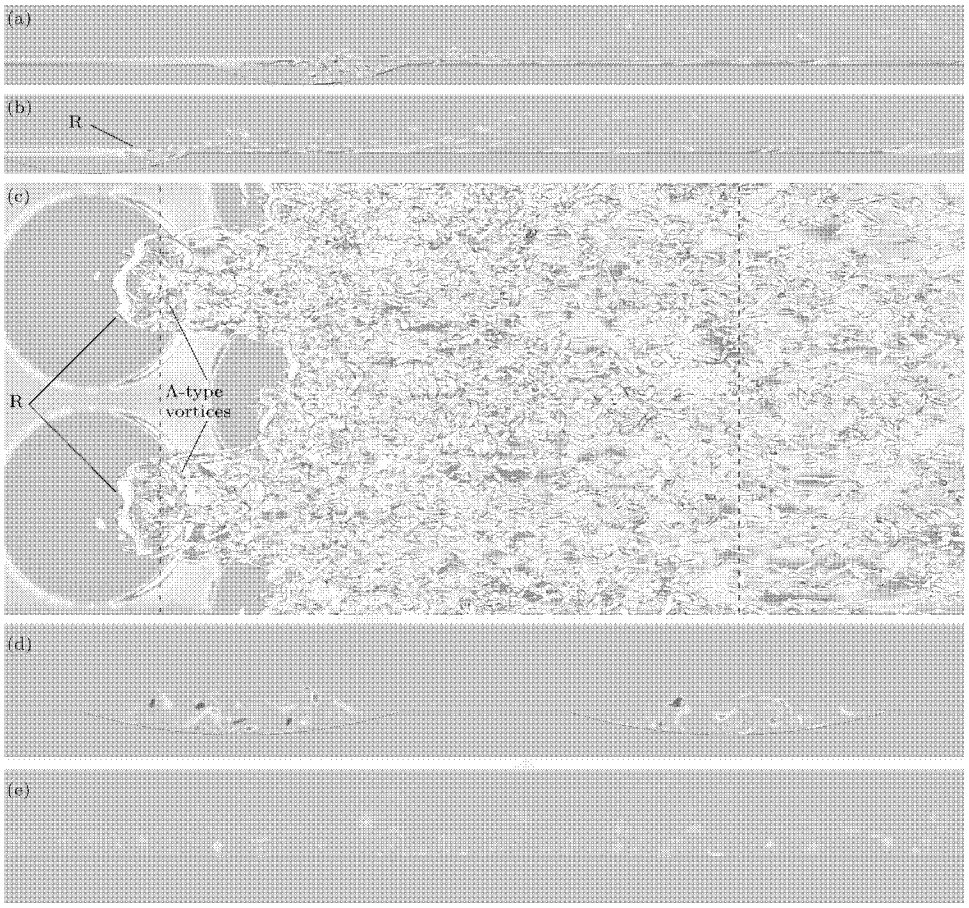

Figure 6. Instantaneous flow visualisation for the case of two rows of dimples. Side views of contours of ω_y at (a) $y/d = 0.0$ and (b) $y/D = 5.5$ passing through the centre of the dimple in the first and second rows, respectively. (c) Top view of an isosurface of the Q criterion with contours of skin friction on the wall. Contours of ω_z at (d) $z/d = 3.5$ and (e) $z/d = 22$ corresponding to the first and second vertical dotted lines above.

a single row of dimples is also shown in Figure 5(a). In this case the shear layer instability over the first row of dimples is similar to the other cases. However the disturbed region is confined to the part of the domain downstream of the dimple and spreads in the spanwise direction slowly. As a result there exists a region between the dimples where the flow is laminar. This laminar region persists some distance downstream as the turbulent activity grows in the spanwise direction and gradually expands to fill the entire domain.

Let us first discuss the origin of the instability and the mechanism by which dimples introduce disturbances into the incoming laminar boundary layer, which is similar for both cases. Figure 6 shows a snapshot of the spanwise vorticity on two planes passing through the centre of the dimples in the first row and second row, respectively. The selected instant in time corresponds to an instant where the shear layer forming over the first row of dimples starts to roll up into a vortical structure, R. The roll-up occurs at a point between the centre and the trailing edge of the dimple. This vortical structure does not extend through the entire span of the dimple, but towards the edges where dimples are more

Downloaded by [University of Delaware] at 07:55 16 October 2014

shallow, the roll-up is suppressed. As a result the spanwise length of vortical structure R is approximately one-third of the dimple diameter D. The roller quickly develops a three-dimensional instability manifested by the bends and kinks seen in Figure 6(c). As the vortical structure R moves downstream and is subjected to local shear, these bends and kinks get stretched and elongated transforming the roller into a packet of Λ-type vortices. We should also note that immediately downstream of vortical structure R, there are pairs of streamwise vortices slanted upwards reminiscent of braid vortices found in free shear layers. A contour plot of the streamwise vorticity ω_z on a vertical $x - y$ plane slicing through the legs of these vortices is shown in Figure 6(d). The plot reveals that the flow inside the dimples is three dimensional consisting of pairs of counter rotating vortices. The braid vortices interact with the rollers and form additional Λ-type vortices of similar scale.

Similar flow behaviour is observed over the second row of dimples with the transformation of a roller into Λ-type vortices. In this case the shear layer roll-up is not as coherent because vortices originating from the first row of dimples pass over the sides. The packet of Λ-type vortices from both dimples propagates downstream and very quickly evolves into a group of hairpin-like vortices over the flat plate. A contour plot of the streamwise vorticity at a location downstream of the dimples (see Figure 6(e)) reveals the presence of streamwise oriented vortices across the entire span of the domain causing significant momentum transport across the boundary layer. The magnitude of the vorticity though is smaller than the streamwise vortices found inside the dimples.

For the case of the eight rows of dimples the flow dynamics over the first two rows of dimples are identical: the shear layer rolls up into a roller which transforms itself into packets of Λ-type vortices evolving downstream (see Figure 7(c)). However the flow dynamics over the third row of dimples and beyond are different. A shear layer forms over the leading edge of the dimples but the roll-up is not coherent and the shear layer rapidly breaks down to smaller vortices. In addition there are vortices originating from the upstream dimples that continue to evolve as they travel over the dimples. A contour plot of the streamwise vorticity on two planes passing through the centre of the third and fourth rows of dimples (see Figure 7(d) and 7(e), respectively) reveals that the flow is populated with streamwise vortices both inside the dimples and above them. The magnitude of the streamwise vorticity of these vortices, however, is higher than that of the vortices over the flat plate (see Figure 6(e)) at the same downstream location indicating that important differences exist between the two cases.

3.2. *Time-averaged statistics*

Having discussed the basic dynamics of some of the instantaneous flow structures we will now look at their footprint on the time-averaged statistics. Figure 8 shows contours of the time-averaged skin friction coefficient $\overline{C_f}$ for the case of the eight rows of dimples (case 2), where the separation line defined as $\overline{C_f} = 0$ is indicated with a solid black line. It can be seen that there is large flow separation covering almost the entire dimple in the first row. In the second row of dimples the separated area is smaller and confined to a small area at the leading edge and around the centre of the dimples. Over the third row of dimples the flow separates over the first half of the dimple, reattaches close to the centre and remains attached after that part. It is interesting that the separation pattern remains unchanged past the second row of dimples, which suggests that the flow dynamics inside the dimples after the first two rows are very similar. Just outside the dimple area the skin friction coefficient rises in the area upstream of the dimple and maintains high values in the post-dimple region.

Downloaded by [University of Delaware] at 07:55 16 October 2014

Downloaded by [University of Delaware] at 07:55 16 October 2014

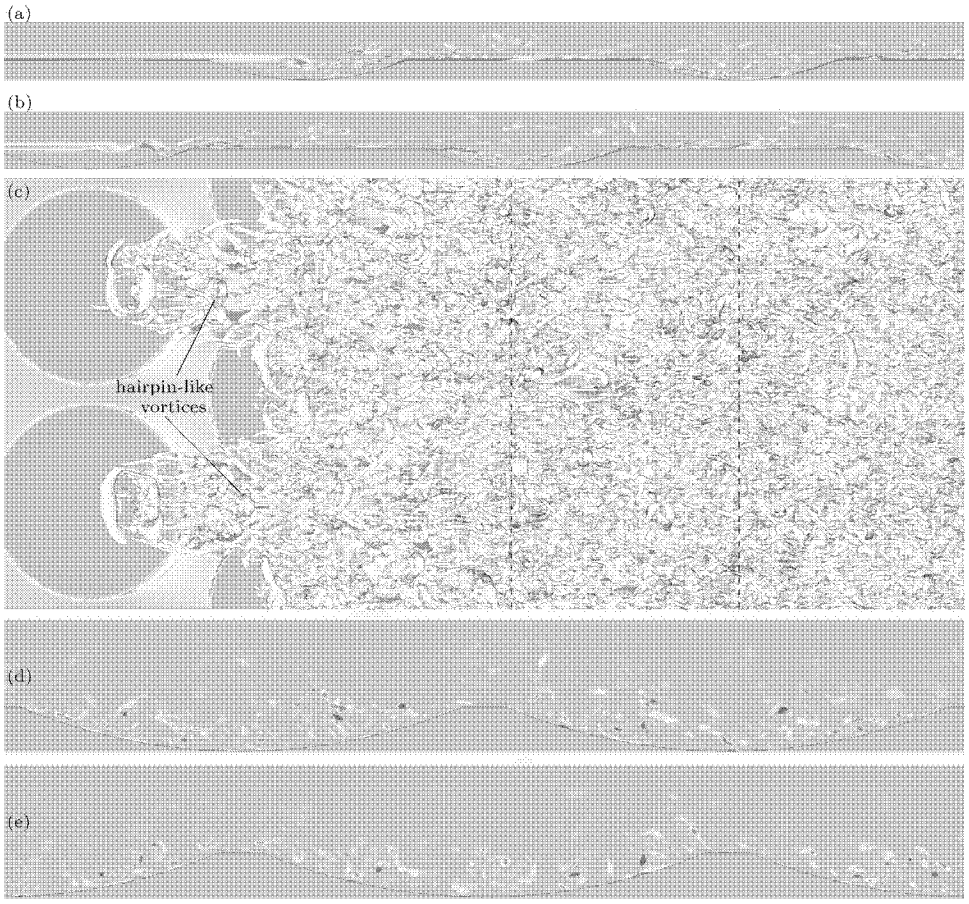

Figure 7. Instantaneous flow visualisation for the case of eight rows of dimples. Side views of contours of ω_y at (a) $y/d = 0.0$ and (b) $y/D = 5.5$ passing through the centre of the dimple in the first and second rows, respectively. (c) Top view of an isosurface of the Q criterion with contours of skin friction on the wall. Contours of ω_z at (d) $z/d = 3.5$ and (e) $z/d = 22$ corresponding to the vertical dotted lines above.

The pressure coefficient along a horizontal line just above the flat plate and passing through the centre of the dimple on the second row is shown in Figure 9. For the dimples on the third row and beyond, the pressure gradient is adverse over more than half of the dimples on the upstream side and then it becomes favourable as the flow accelerates over

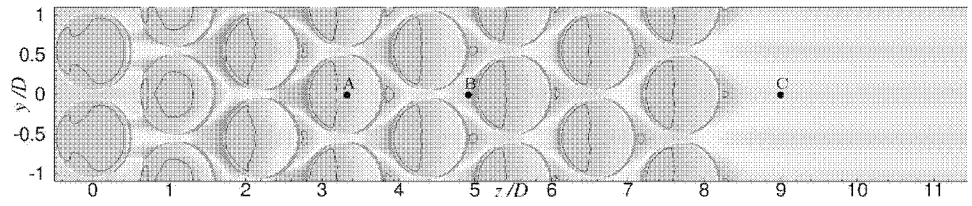

Figure 8. Contour plot of the time-averaged skin friction coefficient $\overline{C}_f$ for the case of eight rows of dimples. The separation line defined as $C_f = 0$ is shown in black.

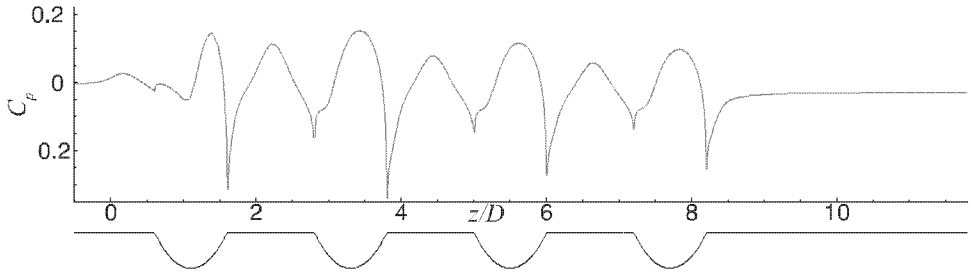

Figure 9. Plot of the time-average pressure coefficient $\overline{C_p}$ for the case of eight rows of dimples along a horizontal line $0.01d$ above the flat plate and passing through the centre of the dimples on the second row ($y = 0$). The outline of the geometry at $y = 0$ is shown below.

Downloaded by [University of Delaware] at 07:55 16 October 2014

the upslope part. It is interesting to note that the pressure coefficient does not remain flat in the area between the dimples but it is affected by the local acceleration of the flow. In particular, the flow decelerates first and accelerates between the trailing edge of one row of dimples and the leading edge of the following row.

The velocity profiles at three locations inside and outside of the dimples are shown in Figure 10 for the two cases. The locations correspond to the positions A,B,C indicated in Figure 8: one inside the dimple centre in the fourth row, one outside the dimple upstream of the sixth row and one inside the boundary layer in the post-dimple region. For the case of the two rows of dimples all points correspond to locations in the post-dimple region and the velocity profiles are reminiscent of a turbulent boundary layer with higher velocity near the wall. For the case of the eight rows of dimples the velocity inside the dimple shown in Figure 10(a) has a less flat shape as a result of the separation bubble and the adverse pressure gradient present in the upstream part of the dimple. Even above the location of the flat plate the velocity profile has less momentum. At the location upstream of the dimples the velocity profile shown in Figure 10(b) recovers and approaches that of two rows of dimples. Finally in the post-dimple region the velocity profile for the case of eight rows of dimples lacks momentum near the wall in comparison with that of two rows of dimples, which suggests that the additional dimples have a significant effect on the momentum transport process. The profiles of the time-averaged streamwise velocity at the same three locations have also been ensemble-averaged in the span and plotted in Figure 11. On the average the behaviour is very similar to the one shown earlier. For most of the locations except at B just upstream

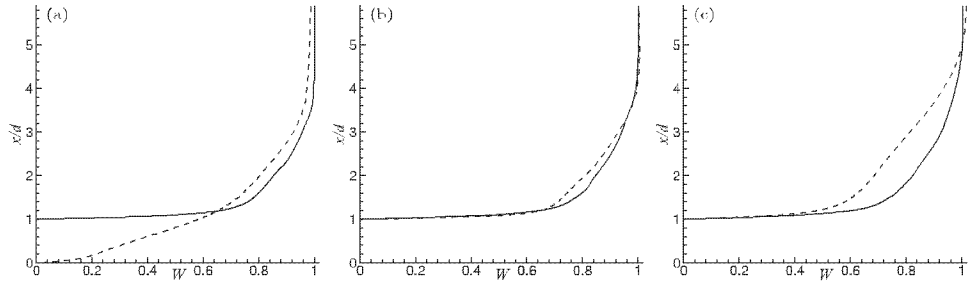

Figure 10. Profiles of the time-averaged streamwise velocity $\overline{W}$ at three locations corresponding to the dots in Figure 8. (a) A, (b) B and (c) C. Lines represent: —— two rows; – – – eight rows.

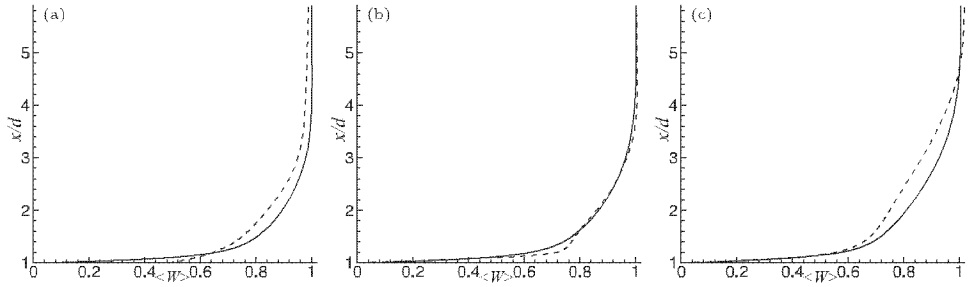

Figure 11. Profiles of the streamwise velocity $<\overline{W}>$averaged over time and spanwise direction at three locations corresponding to the dots in Figure 8. (a), (b) and (c). Lines represent: —— two rows; – – – eight rows.

Downloaded by [University of Delaware] at 07:55 16 October 2014

of the dimples the velocity profiles for the eight rows of dimples exhibit less momentum close to the wall.

The boundary layer parameters for the two cases based on the streamwise velocity $< \overline{W} >$ averaged over time and in the spanwise direction are plotted in Figure 12. The boundary layer thickness is calculated as the point away from the wall where the velocity reaches 99% of the freestream. In both cases the boundary layer grows very rapidly and deviates significantly from the laminar growth of the Blasius solution. By the end of the domain $< \overline{\delta} >$ is at least three times larger than that of a laminar boundary layer. Over the dimples the boundary layer grows in bursts forming very distinct peaks corresponding to the location of the dimple centre in each row followed by valleys in between. The growth of the boundary layer is very different between the two cases downstream of the second row of dimples. For case 1 the boundary layer grows monotonically albeit at a much steeper slope than that of a laminar one. For case 2 the peaks and valleys continue over the subsequent rows with $< \overline{\delta} >$ being significantly larger over a dimple and slightly smaller between the dimples when compared to $< \overline{\delta} >$ at the same location for case 1. Overall by the end of the

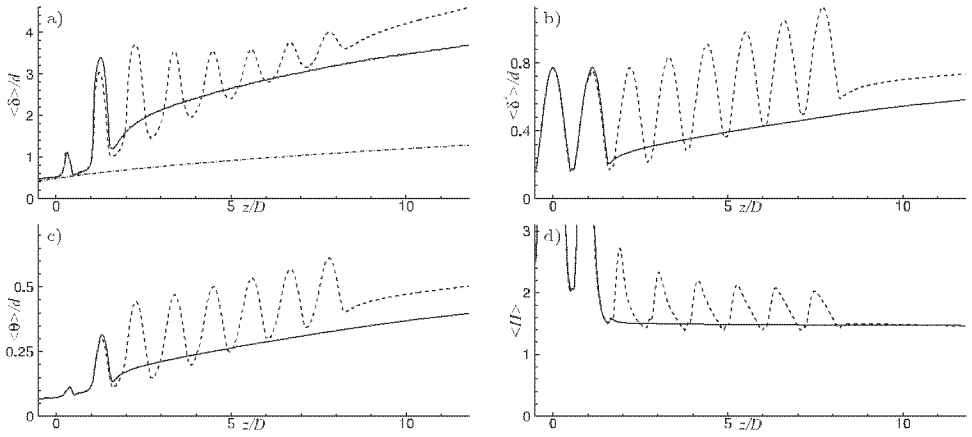

Figure 12. Boundary layer characteristics based on the streamwise velocity $<\overline{W}>$ averaged over time and spanwise coordinate. (a) Boundary layer thickness $<\delta>$, (b) displacement thickness $<\delta^*>$, (c) momentum thickness $<\theta>$ and (d) shape factor $<H> = <\delta^*> / <\theta>$. Lines represent: — two rows; – – –eight rows; – · – Blasius solution.

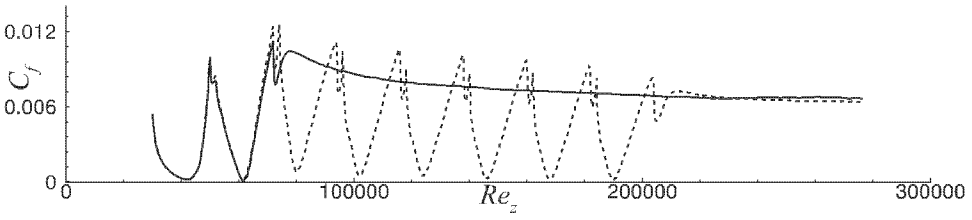

Figure 13. Plot of the skin friction coefficient $<C_f>$ averaged over time and spanwise coordinate versus Re_z based on the distance z from the virtual origin of the flat plate. Lines represent: —— two rows; – – – eight rows.

Downloaded by [University of Delaware] at 07:55 16 October 2014

dimpled part of the plate in case 2, $<\overline{\delta}>$ is consistently higher by about 20% compared to case 1. The behaviour of the displacement thickness, $<\delta^*>$, and momentum thickness, $<\theta>$, is very similar to $<\delta>$. These results indicate the for case 2 the boundary layer has less momentum close to the wall compared to case 1. The shape factor, $<H>$, shown in Figure 12(d) is, however, a little different. A value of $H = 2.59$ is typical of laminar flows, while $H = 1.3-1.4$ is typical of turbulent flows over a zero pressure gradient flat plate. Although $<H>$ is higher over the dimple centre as a result of the adverse pressure gradient, in the post-dimple region $H = 1.5$ for both cases and decreases asymptotically towards $H = 1.4$, which is typical of turbulent boundary layers. That means that despite the differences in the near-wall momentum transport between the two cases, both boundary layers tend towards a turbulent-like state.

The plot of the skin friction coefficient, $<\overline{C_f}>$, averaged over both time and the spanwise coordinate is shown in Figure 13 as a function of Re_{zo}, which is the Reynolds number based on the distance zo from the virtual origin of the boundary layer. For both cases the virtual origin zo is located $20D$ upstream of the leading edge of the first rows of dimples. At that location the corresponding Re_{zo} is 40,000. A zero pressure gradient boundary layer over a smooth wall becomes turbulent at $\mathrm{Re}_{zo} \sim 500{,}000$, while for case 1 a turbulent-like flow is evident (as indicated by the beginning of a negative slope in $<\overline{C_f}>$) and the transition process completes around $\mathrm{Re}_{zo} \sim 80{,}000$. This plot illustrates the dramatic effect that the dimples have on promoting the formation of a turbulent-like boundary layer. Another interesting observation is the behaviour of C_f in the post-dimple region for case 2. Despite the clear differences between the two cases in the region spanning the eight rows of dimples (up to $\mathrm{Re}_{zo} = 210,000$) immediately after the eighth row, C_f for case 2 adjusts very quickly and becomes equal to that of case 1. We should note, however, that for both cases $<\overline{C_f}>$ at the end of the sampling domain, where $\mathrm{Re}_\theta \sim 900$, is still about 40% higher than that of a canonical turbulent boundary layer at the same Re_θ [13]. Profiles of the mean streamwise velocity and turbulent intensities at this location are shown in Figure 14 in inner coordinates. The reference DNS results from [13] at $\mathrm{Re}_\theta = 670$ have also been added for comparison. The mean velocity in both cases has a log-law region but is underpredicted compared to the reference results due to the much higher C_f reported above. The turbulent intensities also resemble qualitatively those of the turbulent boundary layer in [13], with near-wall peaks at the right location, although the magnitude of the intensities is underestimated. Note that away from the wall the turbulent intensities for case 2 decay less rapidly, probably due to the higher activity above the dimples.

To better understand the differences in the flow dynamics between the two cases we look at the budgets of the turbulent kinetic energy k. The transport equation for the turbulent

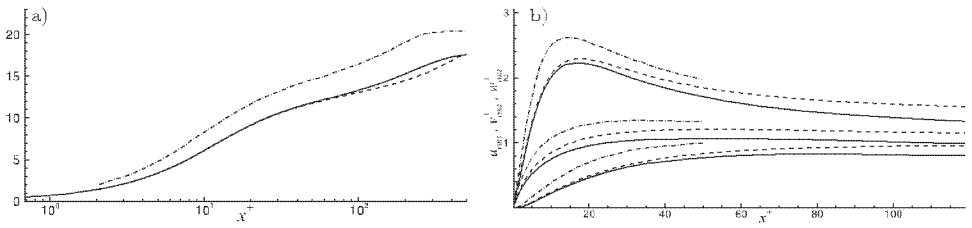

Figure 14. (a) Velocity profile averaged over time and spanwise direction and plotted in wall coordinates. (b) Turbulent intensities. Lines represent: —— two rows at $z/D = 11.8$ ($\mathrm{Re}_\theta = 800$); – – – eight rows at $z/D = 11.8$ ($\mathrm{Re}_\theta = 1000$); – · – turbulent boundary layer ($\mathrm{Re}_\theta = 670$) [13].

Downloaded by [University of Delaware] at 07:55 16 October 2014

kinetic energy, k, is

$$C_k = P_k + T_k + D_k + \Pi_k - \epsilon_k \tag{1}$$

where C_k is the convection, P_k is the production, T_k is the turbulent transport, D_k is the viscous diffusion, Π_k is the velocity pressure gradient and ϵ_k is the dissipation term (see [14] for details). The production and dissipation terms add or remove energy while the remaining terms transport it across the flow. In general, the direction of the transport is determined by the sign of the transport terms: when the transport terms are negative energy is being transported away from that region, while when positive, energy is being transported towards that region. The turbulent kinetic energy, k, budgets averaged over time and the spanwise direction are plotted in Figure 15 at two locations for both cases. One location is at the centre of the fifth row of dimples ($z/D = 5.5$), and one in the post-dimple region ($z/D = 11.8$). For case 1, both locations are in the post-dimple region and all terms in Equation (1) above are similar to the ones for a turbulent channel flow reported in [14].

For case 2 the budget of k at $z/D = 5.5$ (see Figure 15(c)) is very different and resembles more that of a mixing layer (see for example [15]). In this case vertical distance $x/d = 1$ is exactly above the dimple, which is also the reason that P_k, for example, is not zero. The peak in the production term is just above $x/d = 1$, and most of the energy produced at this location is dissipated, while the remaining is transported by the turbulent transport and pressure velocity gradient terms. These terms are negative at $x/d = 1$ but become positive with increasing distance and reach a peak at $x/d = 1.4$. This implies that they transport energy away from the shear layer and towards the outer part of the boundary layer, which is very different from what happens over the smooth part of the plate (see Figure 15(a)): the energy is removed from $x/d = 1.15$ and transported into a region closer to the wall. We should also note that for case 2 the viscous diffusion and convection terms are not very significant at this location. The overall behaviour is consistent with the increased thickness of the boundary layer and enhanced velocity fluctuations away from the wall for case 2. As with C_f above, in the post-dimple region all terms in Equation (1) for case 2 quickly adjust to match those in case 1 at the same streamwise location.

4. Flow around dimpled spheres

The above results indicate that the evolution of the initial perturbation induced by the first two rows of dimples is different over a dimpled surface and over a flat surface. The velocity profiles in Figure 11, for example, clearly show that in the former case there is a considerable momentum deficit in a region close to the wall. To investigate the relevance

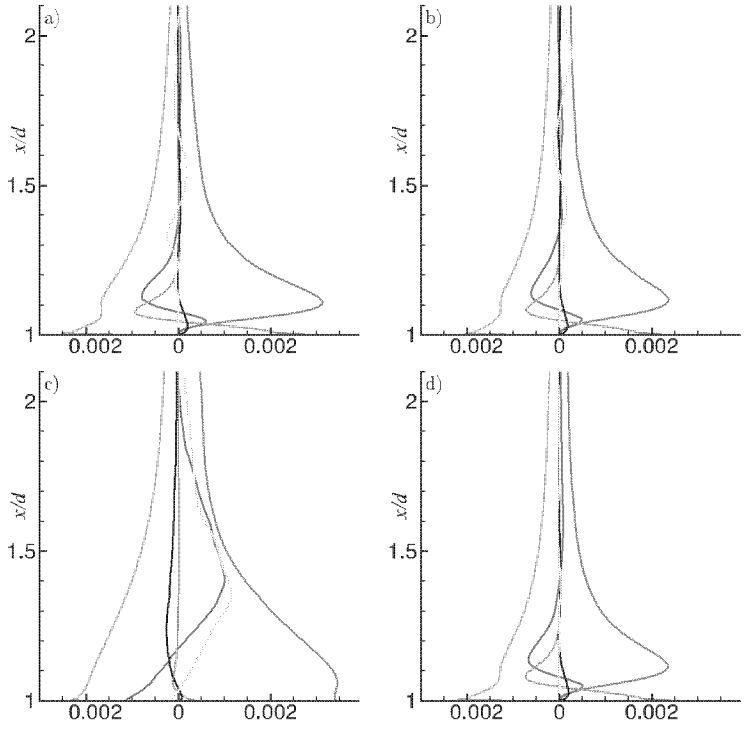

Figure 15. Turbulent kinetic energy budgets as described in Equation (1) for two rows (top figures) and eight rows of dimples (bottom figures). The location correspond to $z = 5.5D$ (left column) and $z = 11.8D$ (right column). Coloured lines represent: $-P_k$; $-\epsilon_k$; $-D_k$; $-T_k$; $-\Pi_k$; $-C_k$.

of this result to separation control applications we considered two cases of flow around dimpled spheres, which are shown in Figure 16. In one case the sphere is covered with approximately 330 dimples, which is typical of a commercial golf ball. In the other case a row of dimples is placed on a smooth sphere along an azimuthal line at an angle $\theta = 60^\circ$ from the front stagnation point. In total there are 30 equally spaced spherical dimples. The dimples in this arrangement serve to trip the boundary layer and the resulting disturbances evolve over a smooth surface. The diameter of the dimples is $D = 0.08D_s$, where D_s is the sphere diameter, and the ratio of dimple depth to dimple diameter is 0.1, which is the same as the one in the flat plate geometries. A cylindrical coordinate grid was employed for these simulations with $1170 \times 1502 \times 3002$ points in the radial, azimuthal and axial directions, respectively. The grid resolution is such that at 45° from the front stagnation point a single dimple is resolved with approximately 140, 67 and 20 points along the tangential, azimuthal and wall-normal directions, respectively. The inflow, outflow and top boundary are located $10D$, $30D$ and $10D$ from the ball, respectively. At the inflow a uniform freestream velocity is specified, at the top boundary a slip-wall is imposed while at the outlet a convective boundary condition is used. The Reynolds number based on the ball diameter is in the super-critical regime, $\mathrm{Re}_D = 110{,}000$. Values obtained for the drag coefficient are within the range of experimental values of similar golf balls found in the literature [1,3]. Details of the numerical set-up and the simulation can be found in [5]. The same grid resolution was utilised in the simulation of the sphere with the single row of dimples.

Downloaded by [University of Delaware] at 07:55 16 October 2014

Downloaded by [University of Delaware] at 07:55 16 October 2014

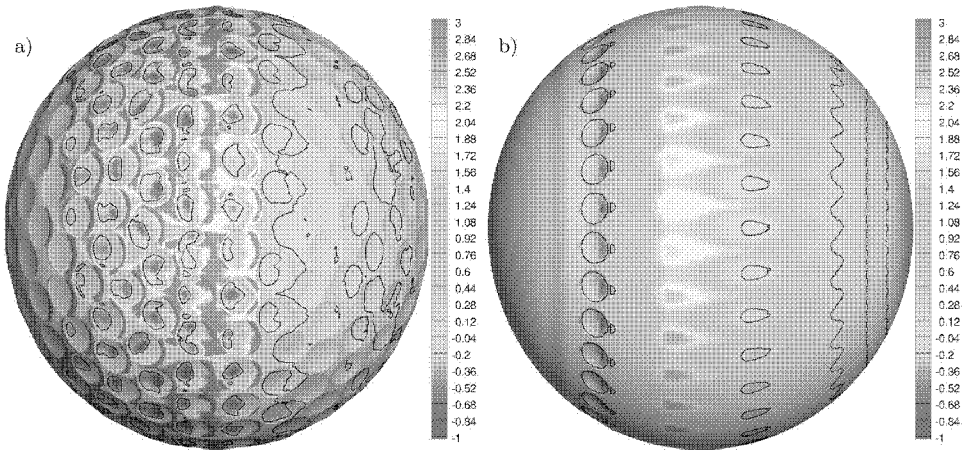

Figure 16. Contour plots of the time-averaged skin friction coefficient Cf scaled by $\mathrm{Re}^{0.5}$ for (a) a typical golf ball and (b) a sphere with one row of dimples at $\theta = 60^\circ$ from the front stagnation point. The solid black line represents the separation line as visualised by $C_f = 0$.

These two cases are qualitatively similar to the flat plate cases discussed earlier. Figure 17(a) shows contours of the instantaneous azimuthal vorticity for the case of one row of dimples on a sphere on an azimuthal plane passing through the centre of one dimple. As in the flat plate cases, the flow separates over the dimple, rolls up and undergoes a complex three-dimensional instability. A turbulent-like boundary layer develops downstream of the dimples where horseshoe-type vortices are present. These vortices cause significant momentum transport across the boundary layer as is evident by an increase of the skin friction coefficient plotted on the surface of the sphere (see Figure 17(b)). As a result the flow at this instant remains attached past 120°.

The dramatic differences of the near-wall flow between the two cases are more evident in the contours of the time-averaged skin friction coefficient shown in Figure 16 (note the separation line, which is shown with a solid black line). In the case of a sphere covered

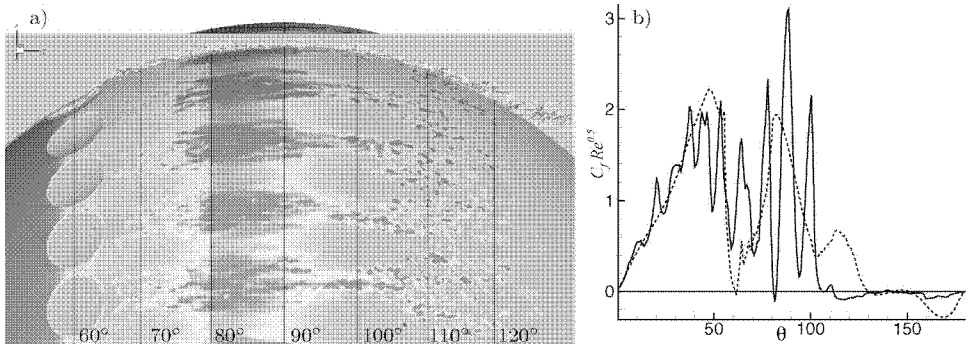

Figure 17. (a) Contour plots of the instantaneous azimuthal vorticity ω_θ and the skin friction coefficient for a sphere with one row of dimples at $\theta = 60^\circ$ from the front stagnation point. (b) Skin friction coefficient averaged over time and azimuthal coordinate. Lines represent: — golf ball; – – – sphere with one row of dimples at $\theta = 60^\circ$.

with dimples the flow separates over the dimples as early as $\theta = 50^\circ$, and the skin friction coefficient reaches very high values at the trailing edge of the dimples and between dimples. Global separation occurs around $\theta = 112^\circ$. For the case of a sphere with a single row of dimples the near-wall flow pattern is significantly different. In this case the flow separates over the entire dimples in the first row. There is a very small recirculation bubble past the trailing edge of the dimples but the flow quickly reattaches and the skin friction coefficient starts to increase in value as transition in the boundary layer takes place. Patches where the skin friction coefficient reaches its maximum value can be seen before $\theta = 90^\circ$. The patches are not uniform in the azimuthal direction and are aligned with the dimples. Past $\theta = 90^\circ$ small separation bubbles form corresponding to areas between the dimples. This is expected as the flow between the dimples is practically laminar and it takes some distance for the turbulent activity originating at the dimples to grow in the azimuthal direction (see Figure 5(a)). However global separation is significantly delayed compared to the dimpled sphere. The plot of $<C_f>$ averaged over both time and azimuthal coordinate clearly shows this point. Although $<C_f>$ exhibits higher peaks for the case of the dimpled sphere the flow separates at $\theta \sim 112^\circ$. For the case of the sphere with one row of dimples global separation occurs at $\theta \sim 120^\circ$.

5. Conclusions

The effect of dimples on a laminar boundary layer has been investigated via DNS of the flow over two rows and eight rows of dimples. In both cases the dimples are effective in tripping the boundary layer towards a turbulent-like state at a very low Reynolds number. It is shown that the shear layer that forms over the first two rows of dimples becomes unstable and rolls up into a coherent vortex sheet. The vortex sheet transforms itself into packet of Λ-type vortices reorienting the spanwise vorticity into streamwise. The dynamics of the flow when these vortices propagate over a flat plate or over a series of dimples are very different. For the first case the flow dynamics resemble that of a zero pressure gradient turbulent boundary layer while for the latter case the local pressure gradient and subsequent shear layer instabilities have a profound effect on the momentum transport across the boundary layer. In particular when multiple rows of dimples are used streamwise vortices with increased strength are found in the dimples which enhance mixing across the boundary layer. As a result the boundary layer grows thicker over the dimples and remains consistently thicker even in the post-dimple region with larger displacement and momentum thicknesses. The budgets of the turbulent kinetic energy also reveal that the dynamics over the dimples resemble more that of a mixing layer where more energy is produced and transported farther away from the flat plate. Computations over dimpled spheres with similar dimple arrangements verify that global separation is indeed delayed when a single row of dimples is used as a trip, which is consistent with the results over the dimpled plates.

Acknowledgements

This work used the Saguaro high-performance computer cluster at ASU's Advanced Computing Center, and the Extreme Science and Engineering Discovery Environment, XSEDE (award TG-CTS110028).

Downloaded by [University of Delaware] at 07:55 16 October 2014

Funding

E. Balaras was partially supported by the National Science Foundation [grant number CBET-0933642].

References

[1] H. Choi, W.P. Jeon, and J. Kim, *Control of flow over a bluff body*, Annu. Rev. Fluid Mech. 40 (2008), pp. 113–139.
[2] E. Achenbach, *Experiments on the flow past spheres at very high Reynolds numbers*, J. Fluid Mech. 54 (1972), pp. 565–575.
[3] P.W. Bearman and J.K. Harvey, *Golf ball aerodynamics*, Aeronautical Q. 27 (1976), pp. 112–122.
[4] J. Choi, W. Jeon, and H. Choi, *Mechanism of drag reduction by dimples on a sphere*, Phys. Fluids 18 (2006), pp. 149–167.
[5] C. Smith, N. Beratlis, E. Balaras, K. Squires, and M. Tsunoda, *Numerical investigation of the flow over a golf ball in the sub-critical and super-critical regimes*, Int. J. Heat Fluid Flow 31 (2010), pp. 402–407.
[6] J. Yang and E. Balaras, *An embedded boundary formulation for large-eddy simulation of turbulent flows interacting with moving boundaries*, J. Comput. Phys. 15 (2006), pp. 12–40.
[7] E. Balaras, *Modeling complex boundaries using an external force field on fixed Cartesian grids in large-eddy simulations*, Comput. Fluids 33 (2004), pp. 375–404.
[8] E. Balaras and J. Yang, *Nonboundary conforming methods for large-eddy simulations of biological flows*, J. Fluids Eng. 127 (2005), pp. 851–857.
[9] P.R. Spalart, *Numerical study of sink flow boundary layers*, J. Fluid Mech. 172 (1986), pp. 307–328.
[10] H. Esmaili and U. Piomelli, *Large-eddy simulation of relaminarizing sink flow boundary layers*, in *Near-Wall Turbulent Flows*, C.G.Speziale, R.M.C. So and B.E. Launder, eds., Elsevier, Amsterdam, 2005, pp. 287–296.
[11] R. Narashima and K.R. Sreenivasan, *Relaminarization in highly accelerated boundary layers*, J. Fluid Mech. 61 (1973), p. 417–447.
[12] J.C.R. Hunt, A.A. Wray, and P. Moin, *Eddies, Stream, and Convergence Zones in Turbulent Flows*, (in its Studying Turbulence Using Numerical Simulation Databases) Proceedings of the 1988 Summer Program, Stanford University, Stanford, CA, 1988, pp. 193–208.
[13] P.R. Spalart, *Direct simulation of a turbulent boundary layer up to Re=1410*, J. Fluid Mech. 187 (1988), pp. 61–98.
[14] N.N. Mansour, J. Kim, and P. Moin, *Reynolds-stress and dissipation-rate budgets in a turbulent channel flow*, J. Fluid Mech. 194 (1988), pp. 15–44.
[15] M.M. Rogers and R.D. Moser, *Direct simulation of a self-similar turbulent mixing layer*, Phys. Fluids 6 (1994), pp. 903–923.

Downloaded by [University of Delaware] at 07:55 16 October 2014